Sensors and Materials, Vol. 36, No. 7 (2024) 2925–2941
MYU Tokyo

S & M 3710

Generative Adversarial Network Applied to Electromagnetic Imaging of Buried Objects

Chien-Ching Chiu,[1*] Wei Chien,[2] Ching-Lieh Li,[1]
Po-Hsiang Chen,[1] Kai-Xu Yu,[1] and Eng-Hock Lim[3]

[1]Department of Electrical and Computer Engineering, Tamkang University, Tamsui 251301, Taiwan
[2]Department of Computer Information and Network Engineering, Lunghwa University of Science and Technology, Taoyuan City 333326, Taiwan
[3]Department of Electrical and Electronic Engineering, University Tunku Abdul Rahman, Kajang 43200, Malaysia

(Received February 2, 2024; accepted June 20, 2024)

Keywords: buried dielectric object, electromagnetic imaging, inverse scattering problems, generative adversarial network

Generative adversarial network (GAN) architecture is employed to tackle the inverse scattering problem of buried dielectric objects in half-space. Traditional iterative methods aimed at resolving the inverse scattering problem of buried dielectric objects have encountered a variety of difficulties, such as highly nonlinear phenomenon, high computational costs for half-space Green's function, and missing measured scattered field information at the lower half of the object. The generator of GAN learns to generate more realistic images, while the discriminator of GAN improves its ability to identify fake images through a game-like process. The iterative process stops when the image generated by the generator is indistinguishable from the real image. In addition, we also analyze and compare the reconstruction outcomes obtained using both GAN and U-Net. Numerical outcomes show that GAN can efficiently reconstruct images with higher reliability than U-Net for buried objects with different dielectric permittivities and handwritten shapes. In summary, our proposed method has opened up a new avenue for imaging buried objects by adopting a deep learning network technique.

1. Introduction

Although many methods are being proposed to solve the electromagnetic inverse scattering (EMIS) problem, real-time data processing and data acquisition, especially for massive objects with high contrasts, are bottlenecks of concern. The aim of EMIS is to obtain imaging information from the measured scattered field. The problem is that its inherent nonlinearity, ill-posedness, and computational cost make it challenging. In the past few decades, EMIS had been widely applied in military measurements and medical inspections. It can be solved by a traditional algorithm or deep learning (DL), where DL can be further categorized into supervised learning and unsupervised learning. The generative adversarial network (GAN) is an innovative approach within the field of machine learning and offers a framework for unsupervised learning,

*Corresponding author: e-mail: chiu@mail.tku.edu.tw
https://doi.org/10.18494/SAM5018

ISSN 0914-4935
https://myukk.org/

generative modeling, adversarial training, feature learning, and data augmentation. Its unique architecture and training methodology have enabled breakthroughs in various applications, making it a prominent and influential aspect of contemporary machine learning research and practice.

Traditional algorithm methods for image reconstruction were previously introduced.[1–11] In 2005, Persico *et al.* proposed the linear model of the Born approximation to reconstruct buried objects. Numerical results showed that the multistate configuration can provide an acceptable compromise between the required measurement time and the computational burden while maintaining the quality of the results. However, this algorithm can only locate the approximate position of the object but cannot reconstruct its shape.[1] Pastorino and Randazzo proposed a Newton algorithm to reconstruct buried objects and evaluated the method's capabilities and limitations from numerical results.[2] In 2019, Chiu *et al.* utilized self-adaptive dynamic differential evolution to reconstruct a buried dielectric object beneath a nonflat rough surface. Numerical results showed that the position of the object and the distribution of the dielectric coefficient can be successfully reconstructed when the noise level is less than 1%.[4] In 2021, Huang *et al.* introduced a full-wave inversion method for reconstructing multiple dielectric parameters of 3D arbitrary anisotropic objects that were buried in layered media. The approach involved utilizing the dielectric parameters obtained from the initial solver as the starting values for the subsequent solver. To reduce computational costs but improve the reconstructed image quality, the inversion domain was systematically downsized using the discrepancies observed between the inverted dielectric parameters and the background. This cascading inversion scheme outperformed the direct arbitrary anisotropic inverse solver and achieved a significant cost saving in computational expenses while producing superior reconstructed images.[8] In 2022, Liang *et al.* presented a novel method called the variational Born iteration technique for reconstructing targets within layered composite structures. This method utilized various orbital angular momentum modes to elevate the precision and excellence of the reconstruction results. By incorporating these modes into the iterative process, the method had prominent success in realizing the targets within the layered composite structures.[9] Later in the same year, Coşğun *et al.* introduced an innovative approach to determine the complex dielectric permittivity profile of 3D inhomogeneous dielectric objects. The method relied on measuring the scattered electric field vectors in the frequency domain. By analyzing the frequency-dependent scattered field data, it became feasible to extract valuable information from the complex dielectric permittivity distribution within the objects of interest. This method offered a promising solution for characterizing the dielectric properties of inhomogeneous materials in three dimensions.[10] Unfortunately, all the abovementioned methods usually took much time to compute the recurring complex Green's functions.

In half-space, objects can be detected in either the time domain or the frequency domain; ground-penetrating radar (GPR) is utilized in the time domain.[12–14] In 2018, Ozkaya and Seyfi proposed a novel algorithm for identifying the concealed scatterer by a multilevel DL approach. The proposed approach employed a new training method to build up its lexica by reconstructing characteristics of the concealed scatterer. Subsequently, different classifiers utilized these lexicons to precisely identify and categorize the detected objects. This algorithm efficiently improved the performance for identifying buried objects in GPR B-scanning via the DL

application.[12] In 2022, Barkataki *et al.* proposed a convolutional neural network (CNN) for predicting the size of buried objects from GPR B-Scans. Numerical results showed that this method has good performance in predicting the buried object size.[13] Wang *et al.* employed a DL method to the scatterer. The reliability of this technology was also assessed through testing and a dataset containing information on underground rainwater pipes. The outcomes showed that the proposed technique was a dependable and precise means of estimating the relative permittivity.[14]

It is worth noting that previous articles focused solely on reconstructing the position or size of the objects, neglecting the shape aspect. To elaborate, GPR utilizes time domain pulses of electromagnetic waves at different frequencies to image buried objects and soil layers. In contrast, our method involves the application of electromagnetic waves at a single frequency. Consequently, reconstructing the object in the frequency domain becomes more challenging.

Among the DL methods, the most prevalent way to solve EMIS problems is U-Net,[15–25] which was proposed for picture-based pixel inverse scattering imaging.[15–17,21] In 2018, Sun *et al.* used CNN to reconstruct diffraction tomography images to solve the multiple scattering problem. Numerical results showed that the proposed DL method possessed the advantage of higher resolution and higher performance than the optimized method.[15] In 2019, Wei and Chen proposed the dominant current scheme (DCS) with CNN to solve the EMIS problem. In the numerical results, three [back-propagation scheme (BPS), DCS, and subspace-based optimization method (SOM)] different initial guesses were input into CNN to reconstruct the microwave images. Results showed that DCS had better noise immunity than BPS and SOM. Unfortunately, the method was not suitable for reconstructing medium and high coefficient distributions.[16] Yao *et al.* proposed a complex-valued DL model for solving the EMIS problem. It consisted of encoder and decoder networks. Numerical results revealed that this approach could solve the EMIS problem accurately even for high-contrast targets. The proposed method provides real-time quantitative microwave imaging for high-contrast scatterers based on DL.[18] In 2021, Li *et al.* proposed the hybrid variational Born iterative method and unsupervised machine learning to solve the inverse scattering problem of multiple objects in layered media. Through the iteration process, the homogeneous scatterer or subscatterer is first classified by unsupervised learning, and then the error between the measured scatter field and reconstructed scatter field is set as the criterion to stop the iteration and discard the background unit. The numerical results confirm that this method can yield good reconstruction results by classifying and reducing the number of unknowns.[20] In 2022, Chiu *et al.* compared the performance of Object-Attentional Super-Resolution Network (OASRN) and U-Net structures in solving EMIS problems. Numerical results showed that OASRN can reconstruct better images than U-Net, but OASRN has the disadvantages of high computational cost and high time consumption.[22] In 2023, Li *et al.* proposed an end-to-end artificial-neural-network-based 2-D electromagnetic full-wave inversion scheme in which different configurations of transceivers were applied during training and testing processes. Several examples were given to verify the feasibility of the proposed method.[24]

Besides U-Net, different neural networks such as GAN and perceptual GAN (PGAN) have been widely applied in many fields recently.[26–31] In 2018, Wang *et al.* proposed a perceptual antagonistic network for image-to-image conversion. Unlike the existing application-driven

algorithms, the perceptual adversarial network provided a general learning framework to map the input image to the desired image and removed the background rainwater image on a rainy day.[26] In 2021, Song *et al.* proposed coarse imaging of the mesoscopic profile by BPS. The resolution of the coarse imaging was enhanced by PGAN. Numerical simulations verified that the proposed method was very effective in achieving fast and high-resolution imaging results compared with other training models. PGAN was good at solving backscattering problems for other physics-related imaging problems as well.[27] Regarding the inverse scattering problem of electromagnetic fields, Guo *et al.* proposed an image transformation network named complex-valued pix2pix that is composed of a generator and a discriminator in 2021. The main improvement of this model was the capability of training optimization by introducing a discriminator to the traditional classic neural network.[28] In 2022, Ye *et al.* used BPS as the initial input for the designed GAN in free space. The proposed method has been proven to be effective in reconstructing objects embedded in an inhomogeneous background.[29] Later, Zhang *et al.* proposed the use of the perceptual mechanism to adjust the GAN to discover the details of the image as well as the edges. To overcome blurred images, the root mean square error, loss function, and perceptual loss function were added to the GAN. Numerical results confirmed that the proposed framework could reconstruct the complete human brain image from computer tomographic data as well as significantly improve the resolution.[30]

To the best of our knowledge, GAN application for buried objects in the frequency domain has not yet been studied. Electromagnetic imaging has multiple scattering effects, resulting in highly nonlinear properties. Compared with full space, the nonlinearity for objects buried in half-space will be more serious owing to the observation angle limitation. The main contribution of this study is the successful reconstruction of the buried object using GAN. A coarse initial dielectric permittivity distribution reconstructed by the BPS method is input to U-Net and GAN and the images reconstructed by these two modules are compared. All the experimental results demonstrate that GAN can generate better images than U-Net.

The structure of this paper is organized as follows. Section 1 is the Introduction. In Sect. 2, we discuss the forward representation of the buried objects. In Sect. 3, the overall flowchart and the structure of GAN are explored. In Sect. 4, we show the numerical results. Conclusions are given in Sect. 5.

2. Forward and Inverse Problem

We imagine a scatterer is buried in a half-space in our simulation environment. (ε_1, σ_1) and (ε_2, σ_2) are the permittivity and conductivity in Regions 1 and 2, respectively. μ_0 denotes the magnetic permeability of free space in Regions 1 and 2. Here, only nonmagnetic substances are being dealt with. The scatterer is assumed to be a cylindrical conductor extending infinitely along the z-axis. The time-dependent relationship of the incident wave is set to be $e^{j\omega t}$ and the incident angle is φ_1, as shown in Fig. 1.

To simplify the analysis, we assume that the transverse magnetic (TM) wave is polarized parallel to the z-axis. The electric field distribution without scatterers is denoted as E_i, which can be expressed mathematically as

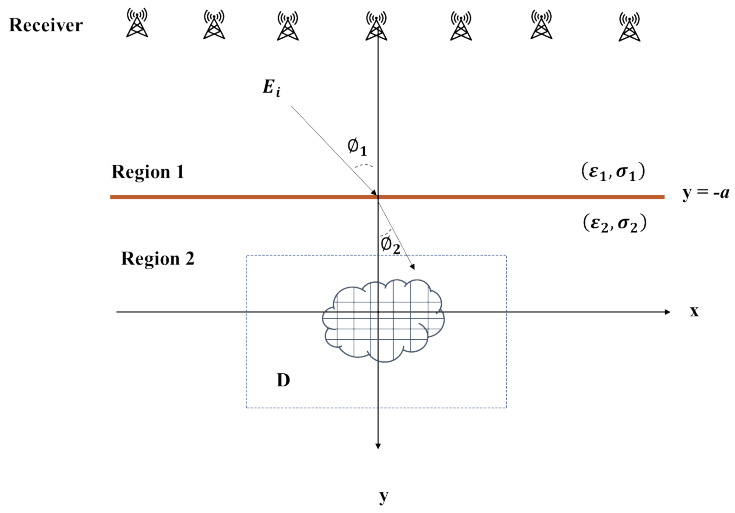

Fig. 1. (Color online) Schematic diagram of two-dimensional buried scatterers in half-space.

$$\vec{E}_i\left(\vec{r}\right) = E_i\left(x, y\right)\hat{z}\,, \tag{1}$$

where

$$E_i\left(x,y\right) = \begin{cases} E_1\left(x,y\right) = e^{-jk_1[x\sin\varphi_1+(y+a)\cos\varphi_1]} + R_1 e^{-jk_1[x\sin\varphi_1-(y+a)\cos\varphi_1]}, & y \le -a \\ E_2\left(x,y\right) = Te^{-jk_2[x\sin\varphi_2+(y+a)\cos\varphi_2]}, & y > -a \end{cases}, \tag{2}$$

$$R_1 = \frac{1-n}{1+n},\ T = \frac{2}{1+n},\quad n = \frac{\cos\varphi_2}{\cos\varphi_1}\sqrt{\frac{\varepsilon_2 - j\sigma_2/\omega}{\varepsilon_1 - j\sigma_1/\omega}}, \tag{3}$$

$$k_1 \sin\varphi_1 = k_2 \sin\varphi_2\,, \tag{4}$$

$$k_i^2 = \omega^2\varepsilon_a\mu_0 - jw\mu_0\sigma_i,\ i = 1, 2,\ Im\left(k_i\right) \le 0\,. \tag{5}$$

$E_1(x, y)$ in the first term of Eq. (2) is the so-called incident field E_i. If Regions 1 and 2 are lossless media, then φ_1 and φ_2 represent the angle of incidence and refraction, respectively. Conversely, if Regions 1 and 2 are lossy media, φ_1 and φ_2 become more complex.

According to the induced current concept and Maxwell's equation, the following equations are obtained:

$$\nabla \times \vec{E} = -j\omega\mu_0\vec{H}\,, \tag{6}$$

$$\nabla \times \vec{H} = -j\omega\varepsilon_0\vec{E} + \vec{j}_{eq}\,, \tag{7}$$

where $\vec{j}_{eq} = j\omega\varepsilon_0 \left[\varepsilon_r (x, y) - \varepsilon_2 \right] E\hat{z}$ is the equivalent current density. The following equation can be obtained using the equivalent current density.

$$E_i(\bar{r}) = \int_s G(r, r') k_2^2 \left[\varepsilon_r (r') - \varepsilon_2 \right] E_t(r') ds' + E_t(r), \; y > -a \tag{8}$$

The scattered field can be written as follows.

$$E_s(\bar{r}) = -\int_s G(r, r') k_2^2 \left[\varepsilon_r (r') - \varepsilon_2 \right] E_t(r') ds' \tag{9}$$

Our buried object is about one wavelength in size. Green's function $G(x, y; x', y')$ must first be solved to seek the correct scattered field for this type of half-space problem. This can be achieved by placing a line current source at (x', y') and the scattered field at (x, y). By the Fourier transform technique, $G(x, y; x', y')$ can be expressed as follows.

$$G(x, y; x', y') = \begin{cases} G_1(x, y; x', y') & , y \le -a \\ G_2(x, y; x', y') = G_f(x, y; x', y') + G_s(x, y; x', y') & , y > -a \end{cases} \tag{10}$$

$$G_1(x, y; x', y') \frac{1}{2\pi} \int_{-\infty}^{\infty} \frac{j}{\gamma_1 + \gamma_2} e^{j\gamma_1 (y+a)} e^{-j\gamma_2 (y'+a)} e^{-j\alpha (x-x')} d\alpha \tag{11}$$

The half-space Green's function can be expressed as

$$G_f(x, y; x', y') = \frac{j}{4} H_0^{(2)} \left[k_2 \sqrt{(x-x')^2 + (y-y')^2} \right], \tag{12a}$$

$$G_s(x, y; x', y') = \frac{1}{2\pi} \int_{-\infty}^{\infty} \frac{j}{2\gamma_2} \left(\frac{\gamma_2 - \gamma_1}{\gamma_2 + \gamma_1} \right) e^{-j\gamma_2 (y+2a+y')} e^{-j\alpha (x-x')} d\alpha, \tag{12b}$$

$$\gamma_i^2 = k_i^2 - \alpha^2, \; i = 1, 2, \; Im(\gamma_i) \le 0, \; y' > a. \tag{13}$$

Here, k_i is the wave number of the i-th region, $G(x, y; x', y')$ is the half-space Green's function, which can be derived using the Fourier transform in Eq. (12a), and $H_0^{(2)}$ is the second-order zero Hankel function. In the numerical method for solving Eqs. (8) and (9), we must compute Green's function in Eq. (10).

Consequently, for buried objects, before feeding traning dataset to the neural network for training, we can perform a noniterative inversion to reconstruct the dielectric permittivity distribution by regression of the scatterer. In the backpropagation method, it is assumed that the electromagnetic field is proportional to the induced current. This enables the effective reconstruction of the scatterer by simplifying the learning process of the GAN during training. We use BPS in the initial image of the guess value.

$$I^b = \chi \cdot [G_1]^* (E_s) \tag{14}$$

The loss function is defined by F^b as

$$F^b(\chi) = (E_s) - [G_1] \cdot \chi \cdot [G_1]^* (E_s)^2 . \tag{15}$$

To find the minimum value of $F(\chi)$, the derivative of $F(\chi)$ is set to be 0. The analytical solution of χ can be written as follows.

$$\chi = \frac{(E_s)^T \cdot [G_1]\left([G_1]^* \cdot (E_s)\right)^H}{\left\| [G_1]\left([G_1]^* \cdot (E_s)\right)\right\|^2} \tag{16}$$

Using χ to derive the induced current from Eq. (14), we can rewrite the total field as

$$\left(E_t^b\right) = (E_i) + [G_1]\left(I^b\right). \tag{17}$$

The equation for the dielectric coefficient (τ) and the induced current I^b is

$$I_p^b = diag\left((\tau_z)^b\right)\left(E_t^b\right), \tag{18}$$

where p represents the incidence.

By combining all incidences of Eq. (18) by the least squares problem technique, the analytic solution is

$$(\tau_z)^b (n) = \frac{\sum_{\rho=1}^{Ni} I_p^b (n) \cdot \left[\left(E_t^b\right)(n)\right]^H}{\sum_{\rho=1}^{Ni} \left\| \left(E_t^b\right)(n)\right\|^2} . \tag{19}$$

3. GAN

With the GAN architecture shown in Fig. 2, we first generate the initial estimated image X by the BPS method. The estimated image X is then input to the generator to generate the output image $G_\theta(X)$. Next, the discriminator is used to discriminate the score between the real image Y and $G_\theta(X)$ as a loss function. Here, θ represents the unknown parameter in the generative network.

In this study, we utilize a five-layer U-Net as the architecture of the GAN generative network. It consists of an expansion network and a contraction network. In the shrinkage network, five sets of convolution, normalization, and ReLu layers are added consecutively. A pooling layer is

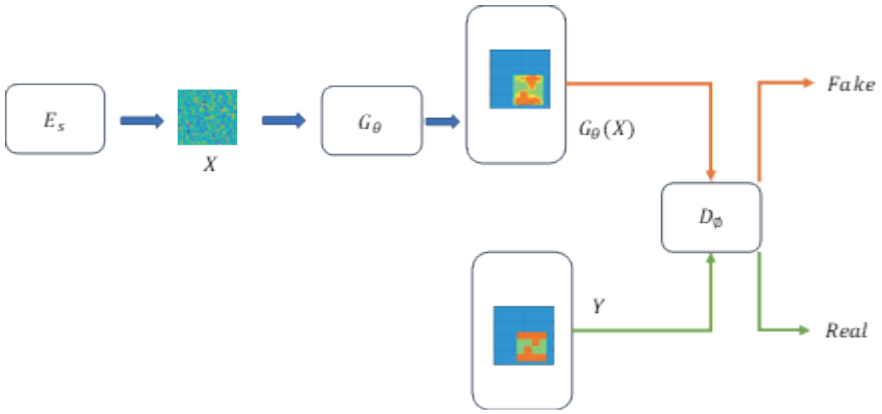

Fig. 2. (Color online) GAN architecture.

then added to shrink the images and their feature values are extracted. In the expansion network section, the Up-convolution layer, normalization layer, and ReLu layer are repeatedly added five times. Through the skip connection connected to each layer, the captured features and the image enlarged by the deconvolution layer are combined and output to the identification network through a 1 × 1 convolution layer, as shown in Fig. 3.

In this paper, $D_\varnothing$ in Fig. 2 denotes the discriminative network and $\varnothing$ is the unknown parameter of the discriminative network. The output of the discriminative network is a discriminative matrix. The generative network is trained alternately with the discriminative network in a mutually resistant manner. The discriminator architecture, which consists of a convolution layer and a ReLu layer, is shown in Fig. 4. The convolution, normalization, and ReLu layers are then added iteratively. The input data of the discriminator is the generated image from the generative network. In other words, the discriminator is evaluated and given a score. The score will then decide whether the generative network needs to update the training weights again. This procedure will cease upon attaining a satisfactory balance.

In GAN, the loss function of the generative network L_{GAN}^{G} is defined as

$$L_{GAN}^{G}\left(\theta\,|\,\varnothing\right)=L_{MSE}\left(\theta\right)+\gamma L_{A}\left(\theta\,|\,\varnothing\right), \tag{20}$$

where $L_{MSE}(\theta)$ is the error between the reconstructed image and the reference image. γ is the weight parameter to balance these two losses. $L_A(\theta|\varnothing)$ is the adversarial loss function of the discriminate network and is expressed as

$$L_{A}\left(\theta\,|\,\varnothing\right)=\frac{1}{N}\sum_{i=1}^{N}\left\|\,D_{\varnothing}\left(G_{\theta}\left(X_{i}\right)\right)-1_{1}\,\right\|. \tag{21}$$

L_A is the scoring mechanism of the discriminative network to determine whether the overall reconstructed image is true or not. N is the amount of data put into the batch.

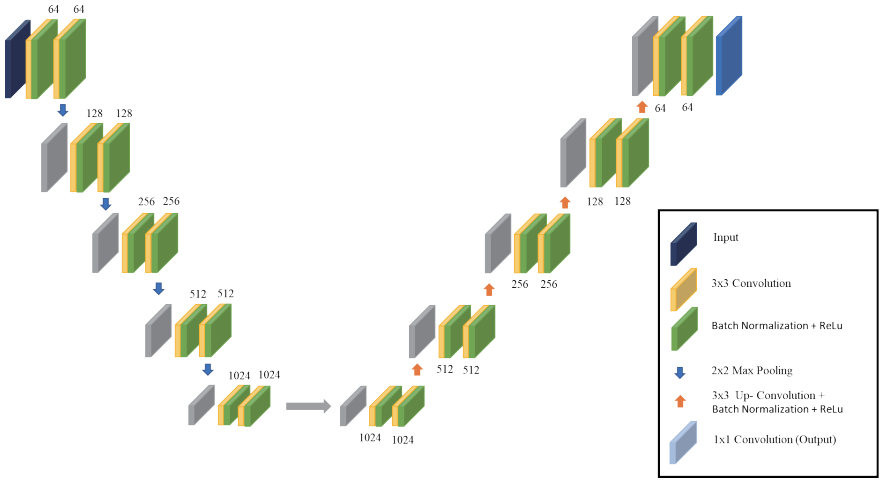

Fig. 3. (Color online) Generator architecture.

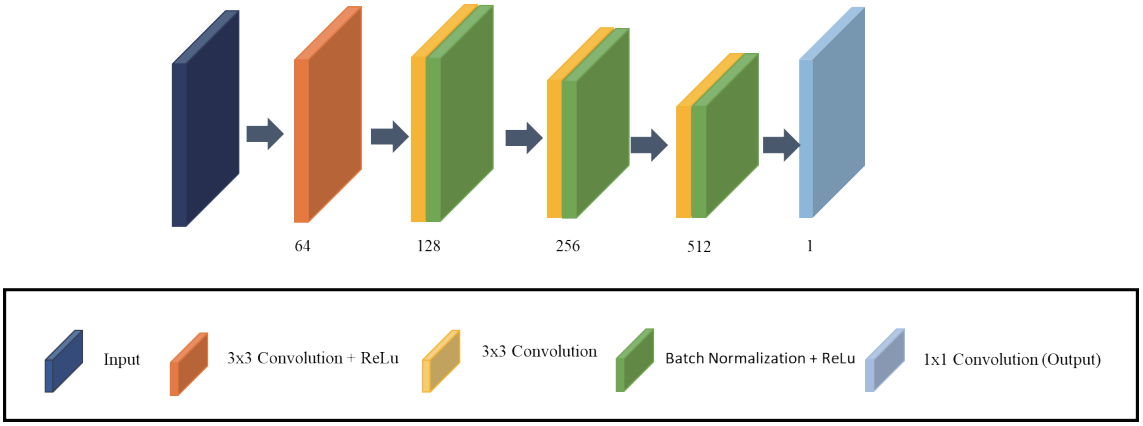

Fig. 4. (Color online) Discriminator architecture.

The loss function of the discriminate network in GAN can be expressed as

$$L_{GAN}^{D}\left(\theta\,|\,\varnothing\right)=\frac{1}{2N}\sum_{i=1}^{N}\left(\left\|D_{\varnothing}\left(Y_i\right)-1\right\|_2^2+\left\|D_{\varnothing}\left(G_{\theta}\left(X_i\right)\right)\right\|_2^2\right), \tag{22}$$

where $\varnothing$ is the unknown amount of parametric data and θ is the weight parameter. Y_i and X_i denote the true and trained data, respectively. Since $D_{\varnothing}$ and G_{θ} are alternately optimized in an adversarial way until a Nash equilibrium is reached, the data generated by the generator $G_{\theta}(X)$ is very close to the real image, and the discriminator $D_{\varnothing}$ cannot distinguish it from the real data. Both the generator and discriminator are powerful enough to reconstruct the distribution of dielectric permittivity.

4. Numerical Results

In this section, we describe the simulation environment developed to conduct numerical analysis of the inverse scattering problem involving dielectric objects buried in a half-space, as depicted in Fig. 1. The incident wave used in the simulations has a frequency of 3 GHz. The buried depth, denoted as a, is set to 0.1 m (one wavelength). In Region 1, the background substance is air, characterized by $\varepsilon_1 = \varepsilon_0$ and $\sigma_1 = 0$. On the other hand, the background substance in Region 2 is soil with $\varepsilon_2 = 2.56$ and $\sigma_2 = 0$. The scatterer is then illuminated with TM polarized plane waves. To introduce variability, different levels of Gaussian noise are added to the simulation environment.

To collect the scattered field information, 32 receivers are positioned around the scatterer, spanning θ_{angle} = 195 to 350° with a radial distance of 3 m. Additionally, 32 transmitters covering the range $\varphi_1 = -80$ to 80° with intervals of 5° are deployed. We test the trained model in four cases. In each case, there are 10 different pictures and 50 random positions. For each example, we calculate the scattered field by the BPS method, and the investigated domain is discretized into 32 × 32 pixels.

We have opted for the widely used adaptive moment estimation (Adam) algorithm during the training process because of its practical effectiveness. Adam can be viewed as a combination of the adaptive gradient algorithm and momentum. One of its advantages is the inclusion of bias correction, which can restrict the learning rate for each iteration, resulting in smoother parameter updates. To ensure training efficiency, we set the initial learning rate to 0.0002 and cut the learning rate in half every 70 epochs. This gradual adjustment aids the fine-tuning of the learning process. Furthermore, we set the momentum parameter to 0.99, which also contributes to the stability and convergence of the training process. A batch size of 32 is chosen to compromise the computational cost and memory requirements. The maximum number of epochs is set to 200 to secure sufficient iterations for model convergence. We shuffle the data at the beginning of each epoch to present diversity and avoid overfitting. The model is evenly exposed to several samples and eliminates possible bias towards specific patterns.

The loss function required in the neural network update is mainly based on the error between the reconstructed image of the buried object and the real image. During the update process, the parameters of the GAN are further updated by the parameters of the discriminator network. Specifically, the proposed GAN method is compared with the U-Net method. Table 1 shows the differentiated loss functions of the two neural network methods. Note that the weight parameter γ for L_{GAN}^{G} in Eq. (20) is set to 0.001.

To quantitatively evaluate the reconstruction accuracy of all methods, the structure similarity index measure (SSIM) in Eq. (23) and the normalized root-mean-square error (NRMSE) in Eq. (24) are taken as the quality metrics.

Table 1
Loss function for U-Net and GAN.

Method	U-Net	GAN
Loss	$L_{U\text{-}Net}(\theta) = L_{MSE}(\theta)$	$L_{GAN}^{G}(\theta\|\varnothing) = L_{MSE}(\theta) + \gamma L_A(\theta\|\varnothing)$

To calculate the numerical result of each program by GAN, we define the NRMSE formula as

$$RMSE = \frac{1}{M}\sum_{i=1}^{M} \left|\left| Y - Y^{r} \right|\right|_{F} / \left|\left| Y \right|\right|_{F} , \tag{23}$$

where Y and Y^{r} represent the real shape and the reconstructed shape, respectively, M is the total test numbers, and F is the Frobenius norm.

To compare the reconstruction result of each numerical result trained by GAN, we define the SSIM formula as[23]

$$SSIM = \frac{\left(2\mu_{\tilde{y}}\mu_{y} + C_{1}\right)\left(2\sigma_{\tilde{y}y} + C_{2}\right)}{\left(\mu_{\tilde{y}}^{2} + \mu_{y}^{2} + C_{1}\right)\left(\sigma_{\tilde{y}}^{2} + \sigma_{y}^{2} + C_{2}\right)} . \tag{24}$$

SSIM is a measure mainly used to indicate the similarity of two images of the same size or the degree of distortion of an image. In most papers, SSIM is used to compare the brightness, contrast, and structure of two images separately, and then these three elements are weighted to express them as a product.

4.1 GAN and U-Net for dielectric coefficient from 3 to 3.5

In this scenario, we set the distribution of the dielectric coefficient to a range between 3 and 3.5. Our simulated environment includes a total of 32 transmitters and 32 receivers. For the sake of real adaption, we introduce 20% Gaussian noise to the scattered field measurements. We assume that the scatterers occupy 10 distinct dielectric permittivity distributions, and they can be located at any of the 50 positions within the measurement area. As a result, the dataset comprises a total of 500 images in each case. We divide the dataset into two subsets to facilitate the training and evaluation processes: 80% for training and 20% for testing. The distribution estimated by the BPS method is then input to both GAN and U-Net models for comparison. Figure 5(a) shows the extracted image. Figures 5(b) and 5(c) show the reconstruction results of U-Net and GAN, respectively, with 20% noise added to the simulation environment. NRMSE and SSIM for the reconstruction results are tabulated in Table 2. The edges on the upper part of the image reconstructed by U-Net are blurred and unclear, while the image reconstructed by GAN is clearer. From these results, we conclude that GAN is superior to U-Net in reconstructing the distribution of dielectric permittivity.

4.2 GAN and U-Net for dielectric coefficient from 3.5 to 4

For this scenario, we define the distribution of the dielectric coefficient as a range between 3.5 and 4. As in the previous case, 32 transmitters and 32 receivers are deployed in the simulated environment. However, in this scenario, we introduce 10% Gaussian noise to the scattered field measurements. Meanwhile, both the training and testing sets remain identical to those used in

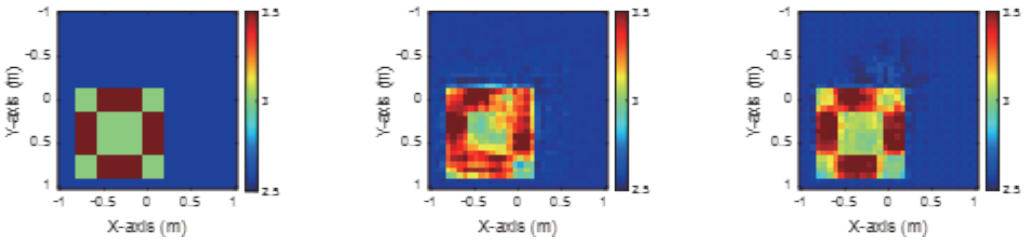

(a) (b) (c)

Fig. 5. (Color online) Dielectric coefficient from 3–3.5. (a) Extracted image. (b) Reconstructed image by U-Net. (c) Reconstructed image by GAN.

Table 2.
NRMSE and SSIM of relativity permittivity from 3 to 3.5 with 20% noise, reconstructed by U-Net and GAN.

Method	U-Net(%)	GAN(%)
NRMSE	4.5	3.8
SSIM	86.8	90.6

Sect. 4.1 (trained model) to ensure consistency and fair evaluation. To estimate the preliminary dielectric permittivity distribution, we use the BPS method. The estimated result is subsequently fed into both GAN and U-Net models for comparison. Figure 6(a) shows the extracted image. Figures 6(b) and 6(c) show the reconstruction results of U-Net and GAN, respectively, with 10% noise added to the simulation environment. NRMSE and SSIM for the reconstruction results are given in Table 3. It is seen that the dielectric permittivity in the inner part of the image reconstructed by U-Net is blurred, but is clearer in the GAN image. The results reveal that GAN reconstructs the distribution of permittivity better than U-Net in the inner part of the image.

4.3 GAN and U-Net for dielectric coefficient from 4 to 4.5

In this case, we set the dielectric coefficient distribution between 4 and 4.5. Again, 32 transmitters and 32 receivers are placed in the simulated environment. 5% Gaussian noise is added to the scattered field. The training and test sets are the same as in the previous two cases. We apply BPS to estimate the preliminary permittivity distribution and then feed it into GAN and U-Net. Figure 7(a) shows the extracted image. Figures 7(b) and 7(c) show the reconstruction results of U-Net and GAN, respectively, with 5% noise added to the simulation environment. NRMSE and SSIM for the reconstruction results are listed in Table 4. The simulation results show that the dielectric permittivity distribution on the upper left and lower right at the inner parts of the reconstructed image by U-Net are blurred, but they are clearer in the reconstructed image by GAN. Apparently, GAN is able to reconstruct the distribution of permittivity better than U-Net.

4.4 Modified national institute of standards and technology database (MNIST)

The MNIST serves as a comprehensive repository for handwriting recognition tasks. It encompasses an extensive collection of handwritten digits ranging from 0 to 9. Each image in

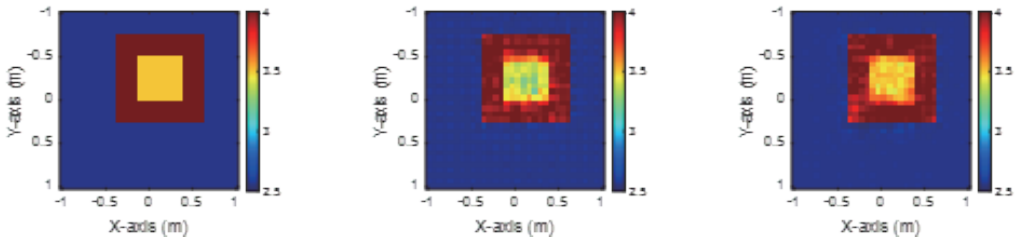

(a) (b) (c)

Fig. 6. (Color online) Dielectric coefficient from 3–3.5. (a) Extracted image. (b) Reconstructed image by U-Net. (c) Reconstructed image by GAN.

Table 3
NRMSE and SSIM of relativity permittivity from 3.5 to 4 with 10% noise, reconstructed by U-Net and GAN.

Method	U-Net(%)	GAN(%)
NRMSE	3.5	3.0
SSIM	80.5	92.3

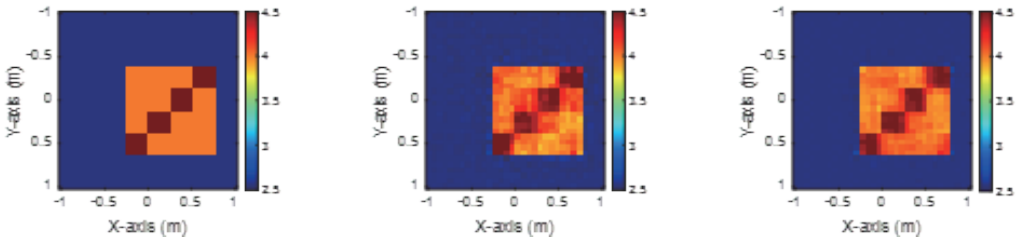

(a) (b) (c)

Fig. 7. (Color online) Dielectric coefficient from 4–4.5. (a) Extracted image. (b) Reconstructed image by U-Net. (c) Reconstructed image by GAN.

Table 4
NRMSE and SSIM of relativity permittivity from 4 to 4.5 with 5% noise, reconstructed by U-Net and GAN.

Method	U-Net(%)	GAN(%)
NRMSE	3.8	3.0
SSIM	90.0	91.4

the database is of size 28 × 28 pixels. There are 10000 images for each digit. It contains different handwriting styles, each with a different angle rotation. Because of its accessibility and rich content, MNIST has become a popular choice for training and evaluating image processing network architectures, particularly those based on neural networks. Researchers and developers leverage this database to fine-tune and optimize their models for tasks related to handwriting recognition and similar image processing applications. The availability and standardization of MNIST have considerably facilitated advancements in this field, allowing for the exploration of innovative approaches and the development of more accurate and efficient image processing algorithms.

We select 500 images from MNIST for training and distribute the dielectric coefficient between 3 and 4.5. We apply BPS to estimate the preliminary permittivity distribution and then

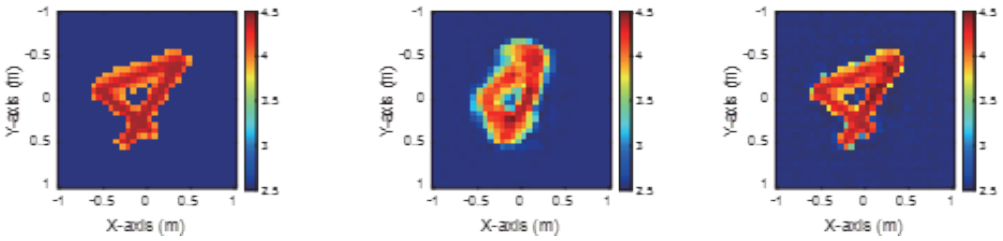

(a) (b) (c)

Fig. 8. (Color online) MNIST samples of permittivity from 3–4.5. (a) Extracted image. (b) Reconstructed image by U-Net. (c) Reconstructed image by GAN

Table 5
NRMSE and SSIM of relativity permittivity 3 to 4.5 for MNIST samples reconstructed by U-Net and GAN.

Permittivity	3 to 3.5		3.5 to 4		4 to 4.5	
Method	U-Net(%)	GAN(%)	U-Net(%)	GAN(%)	U-Net(%)	GAN(%)
NRMSE	5.29	4.1	7.7	7.1	9.6	8.5
SSIM	83.60	86.7	81.5	84.1	80.2	82.6

input it to U-Net and GAN. One hundred MNIST samples are then randomly selected to run the test. The reconstruction results of U-Net and GAN are shown in Fig. 8. The results show that GAN performs better than U-Net. NRMSE and SSIM of the reconstruction results are given in Table 5. As seen, the middle part is blurred for digit 9 reconstruction by U-Net. However, the reconstruction result by GAN is clearer. For digit 2, the lower part reconstructed by U-Net is blurred, but the overall contour of the GAN reconstruction is more complete. Like digit 2, the lower part of digit 4 reconstructed by U-Net is blurred. Again, GAN reconstruction appears to be better than U-Net reconstruction.

In summary, the experimental data validate our proposed approach. GAN is more suitable for highly nonlinear problems than U-Net and has better performance and accuracy with different levels of added noise. The total training times for GAN and U-Net are 90 and 65 min, respectively, on a personal computer with Intel i7-12700, 3060ti GPU, and 32 GB of memory. Note that all simulations have the same parameters in the same environment. Although GAN takes a longer time to train the model and requires more memory for training, it is capable of reconstructing a clearer image.

5. Conclusions

In this paper, we propose a new DL method to reconstruct buried objects using GAN. In the first step, a coarse initial image is reconstructed by BPS and then input to the GAN. The loss function of GAN consists of a generative network and a discriminator network. The discriminator evaluates the similarity between the reconstructed image and the real image, allowing the generator to reconstruct more accurate images. A series of experimental data verify that the proposed GAN can effectively improve the accuracy and generalization of the reconstruction performance compared with U-Net. Simulation results have proved the possibility of resolving buried permittivity with high precision, even for scatterers with extremely high

contrast. Numerical benchmarks have further confirmed the effectiveness and validity of the proposed approach. In summary, GAN has proven to be a novel and efficient means of achieving the real-time quantitative microwave imaging of buried objects, which is the major contribution of this research.

References

1 R. Persico, R. Bernini, and F. Soldovieri: IEEE Trans. Antennas Propag. **53** (2005) 1875. https://doi.org/10.1109/TAP.2005.848468
2 M. Pastorino and A. Randazzo: Int. J. Micro. Sci. Technol. **2012** (2012) 637301. https://doi.org/10.1155/2012/637301
3 Z. Miao and P. Kosmas: IEEE Trans. Antennas Propag. **65** (2017) 2507. https://doi.org/10.1109/TAP.2017.2679067
4 C.-C. Chiu, G.-Z. Lee, H. Jiang, and B.-J. Hong: J. Electron. Waves Appl. **33** (2019) 1905. https://doi.org/10.1080/09205071.2019.1653229
5 T. Yin, Z. Wei, and X. Chen: IEEE Trans. Antennas Propag. **68** (2020) 4764. https://doi.org/10.1109/TAP.2020.2969708
6 C. Yang, J. Zhang, and M. S. Tong: IEEE Trans. Antennas Propag. **69** (2021) 1078. https://doi.org/10.1109/TAP.2020.3008672
7 A. Sefer and A. Yapar: IEEE Trans. Geosci. Remote Sens. **59** (2021) 1041. https://doi.org/10.1109/TGRS.2020.2997637
8 X. Huang, J. Li, J. Zhuo, F. Han, and Q. H. Liu: IEEE Geosci. Remote Sens. Lett. **19** (2021) 8011805. https://doi.org/10.1109/LGRS.2021.3076433
9 B. Liang, F. Shen, S. M. Wang, Y. Zhou, Y. Yang, K. Cheng, and Y. Gong: Phys. Rev. E **105** (2022) 025302. https://doi.org/10.1103/PhysRevE.105.025302
10 S. Coşğun, E. Bilgin, and M. Çayören: IEEE Trans. Antennas Propag. **70** (2022) 4810. https://doi.org/10.1109/TAP.2022.3140527
11 K. Ren and R. J. Burkholder: IEEE Geosci. Remote Sens. Lett. **19** (2022) 4500205. https://doi.org/10.1109/LGRS.2020.3037014
12 U. Ozkaya and L. Seyfi: Signal, Image Video Process. **12** (2018) 1567. https://doi.org/10.1007/s11760-018-1313-x
13 N. Barkataki, B. Tiru, and U. Sarma: J. Applied Geophys. **200** (2022) 104620. https://doi.org/10.1016/j.jappgeo.2022.104620
14 H. Wang, S. Ouyang, Q. Liu, K. Liao, and L. Zhou: Remote Sens. **14** (2022) 4293. https://doi.org/10.3390/rs14174293
15 Y. Sun, Z. H. Xia, and U. S. Kamilov: Opt. Exp. **26** (2018) 14678. https://doi.org/10.1364/OE.26.014678
16 Z. Wei and X. Chen: IEEE Trans. Geosci. Remote Sens. **57** (2019) 1849. https://doi.org/10.1109/TGRS.2018.2869221
17 A. Massa, D. Marcantonio, X. Chen, M. Li, and M. Salucci: IEEE Antennas Wirel. Propag. Lett. **18** (2019) 2225. https://doi.org/10.1109/LAWP.2019.2916369
18 H. M. Yao, W. E. I. Sha, and L. Jiang: IEEE Antennas Wirel. Propag. Lett. **18** (2019) 2254. https://doi.org/10.1109/LAWP.2019.2925578
19 K. Xu, L. Wu, X. Ye, and X. Chen: IEEE Trans. Antennas Propag. **68** (2020) 7457. https://doi.org/10.1109/TAP.2020.2998171
20 J. Li, Y. Chen, J. Zhuo, and F. Han: IEEE Trans. Geosci. Remote Sens. **60** (2022) 2002212. https://doi.org/10.1109/TGRS.2021.3089631
21 M. Salucci, M. Arrebola, T. Shan, and M. Li: IEEE Trans. Antennas Propag. **70** (2022) 6349. https://doi.org/10.1109/TAP.2022.3177556
22 C. C. Chiu, T. H. Kang, P. H. Chen, H. Jiang, and Y. K. Chen: J. Electron. Waves Appl. **37** (2022) 93. https://doi.org/10.1080/09205071.2022.2113444
23 C. C. Chiu, P. H. Chen, and H. Jiang: IEEE Trans. Geosci. Remote Sens. **60** (2022) 208414. https://doi.org/10.1109/TGRS.2022.3222502
24 J. Li, H. J. Hu, J. Wang, M. Zhuang, L. Y. Xiao, and Q. H. Liu: IEEE Trans. Antennas Propag. **71** (2023) 4600. https://doi.org/10.1109/TAP.2023.3254131
25 H. H. Zhang, H. M. Yao, L. Jiang, and M. Ng: IEEE Trans. Antennas Propag. **71** (2023) 2867. https://doi.org/10.1109/TAP.2023.3239185

26 C. Wang, C. Xu, C. Wang, and D. Tao: IEEE Trans. Image Process. **27** (2018) 4066. https://doi.org/10.1109/TIP.2018.2836316
27 R. Song, Y. Huang, K. Xu, X. Ye, C. Li, and X. Chen: IEEE Trans. Comput. Imag. **7** (2021) 689. https://doi.org/10.1109/TCI.2021.3093793
28 L. Guo, G. Song, and H. Wu: Electronics **10** (2021) 752. https://doi.org/10.3390/electronics10060752
29 X. Ye, N. Du, D. Yang, X. Yuan, R. Song, S. Sun, and D. Fang: IEEE Trans. Antennas Propag. **70** (2022) 8262. https://doi.org/10.1109/TAP.2022.3164198
30 K. Zhang, H. Hu, K. Philbrick, G. M. Conte, J. D. Sobek, P. Rouzrokh, and B. J. Erickson: Tomography **8** (2022) 905. https://doi.org/10.3390/tomography8020073
31 R. Song, Y. Huang, X. Ye, K. Xu, C. Li, and X. Chen: IEEE Trans. Antennas Propag. **70** (2022) 6218. https://doi.org/10.1109/TAP.2021.3139645

About the Authors

Chien-Ching Chiu received his B.S.C.E. degree from National Yang Ming Chiao Tung University, Hsinchu, Taiwan, in 1985, and M.S.E.E. and Ph.D. degrees from National Taiwan University, Taipei, Taiwan, in 1987 and 1991, respectively. From 1987 to 1989, he was a communication officer with the ROC Army Force, Taoyuan, Taiwan. In 1992, he joined the Department of Electrical Engineering, Tamkang University, Taipei, where he is currently a professor. From 1998 to 1999, he was a Visiting Scholar at the Massachusetts Institute of Technology, Cambridge, MA, USA, and the University of Illinois at Urbana-Champaign, Champaign, IL, USA. He was a Visiting Professor at the University of Wollongong, Wollongong, NSW, Australia, in 2006, the University of Queensland, Brisbane, QLD, Australia, in 2007, the University of London, London, U.K., in 2011, and University Tunku Abdul Rahman, Kampar, Malaysia, from 2019 to 2020. He has authored more than 170 journal articles on inverse scattering problems, communication systems, and optimization algorithms. His current research interests include inverse problems, deep learning for microwave imaging, indoor wireless communications, and simultaneous wireless information and power transfer systems. Dr. Chiu is listed as one of the World's Top 2% Scientists 2021–2023 by Stanford University. (chiu@mail.tku.edu.tw)

Wei Chien received his B.S.C.E. degree from Ta Tung University, Taipei, in 1997 and his M.S.E.E. degree from Tamkang University, Taipei, in 1999. From 1999 to 2001, he served in the ROC Army Force and was an assistant in the Department of Electrical Engineering. From 2007 to 2014, he was an assistant professor in the Department of Electronic Engineering, De Lin Institute of Technology. From 2014 to 2017, he was a professor in the Department of Computer Engineering, Ningde Normal University. Since 2017, he has been a professor in the Department of Electric and Information Engineering, Beibu Gulf University. His research area is deep learning for inverse scattering. (air180@seed.net.tw)

Ching-Lei Li received his B.S. degree from National Taiwan University, Taipei, Taiwan, in 1985, and M.S. and Ph.D. degrees from Michigan State University, East Lansing, in 1990 and 1993, respectively, all in electrical engineering. From 1989 to 1993, he was a research assistant in the Electrical Engineering Department, Michigan State University, where he worked on measurement techniques for determining the electromagnetic properties of materials. In 1993, he joined the Electrical Engineering Faculty at Tamkang University, Taipei, where he is now a professor. Currently, his research activities involve the inverse scattering problem, microstrip antenna design, and dielectric material characterization. His areas of special interest include theoretical and computational electromagnetics, the application of various optimization schemes, such as the steady-state genetic algorithm, particle swarm optimization, differential evolution, and Taguchi method, to electromagnetics, recent emerging research areas including applications of artificial intelligence in electromagnetics, and other topics.
(chingliehli1001@gms.tku.edu.tw)

Po-Hsiang Chen received his B.S. degree from HungKuo Delin University of Technology, Tucheng, Taiwan, in 2017 and M.S. degree from Tamkang University, Tamsui, Taiwan, in 2020. Since 2021, he has been working toward his Ph.D. degree at the Department of Electrical and Computer Engineering, Tamkang University, Tamsui, Taiwan. His research areas are inverse scattering and deep learning. (810440031@gms.tku.edu.tw)

Kai-Xu Yu received his B.S. degree from Tamkang University, Tamsui, Taiwan, in 2020 and M.S. degree from Tamkang University, Tamsui, Taiwan, in 2023. His research areas are inverse scattering and deep learning. (610440108@gms.tku.edu.tw)

Eng-Hock Lim received his B.Sc. degree in electrical engineering from National Taiwan Ocean University in 1997, M.Eng. degree in electrical and electronic engineering from Nanyang Technological University in 2000, and Ph.D. degree in electronic engineering from the City University of Hong Kong in 2007. He is currently a professor at Universiti Tunku Abdul Rahman (UTAR). He was the Founding Chair of the IEEE Malaysia Council on RFID. He served as an associate editor for IEEE Transactions on Antennas and Propagation from 2013 to 2016. He is currently serving as an associate editor for the IEEE Journal of Radio Frequency Identification. Since April 2021, he has been a Distinguished Lecturer of the IEEE Council on RFID. He is a fellow of the Academy of Sciences Malaysia and the ASEAN Academy of Engineering and Technology. His current research interests include RFID antennas, smart and re-configurable antennas, and multifunctional antennas. (limeh@utar.edu.my)